

Enhanced oxygen reduction reaction catalyst stability and durability of MXene-supported Fe-N-C catalyst for proton exchange membrane

Norhamizah Hazirah Ahmad Junaidi¹, Wai Yin Wong^{1*}, Kee Shyuan Loh¹, Rahman Saidur^{2,5}
and Thye Foo Choo³, Wu Bo⁴

¹*Fuel Cell Institute, Universiti Kebangsaan Malaysia, 43600 Bangi, Selangor, Malaysia*

²*Research Centre for Nano-Materials and Energy Technology, School of Engineering and
Technology, Sunway University, Jalan Universiti, Bandar Sunway, 47500 Petaling Jaya,
Selangor, Malaysia*

³*Malaysian Nuclear Agency, Bangi, 43000 Kajang, Selangor, Malaysia*

⁴*H2Green (Ningbo) New Energy Technology Co., Ltd. 3F, Building 17, Fugang Electronic
Commerce Mall, No. 5000 Airport Road, Shiqi Subdistrict, Haishu District, Ningbo City,
Zhejiang Province, China.*

⁵*School of Engineering, Lancaster University, Lancaster, LA1 4YW, UK*

*Corresponding author: waiyin.wong@ukm.edu.my

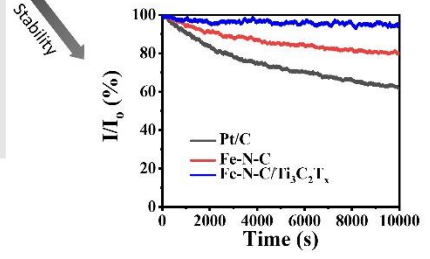
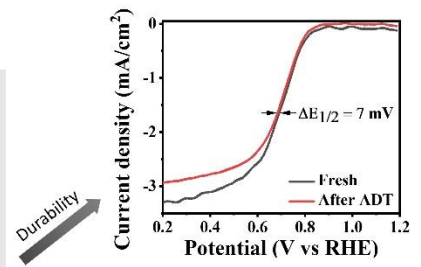
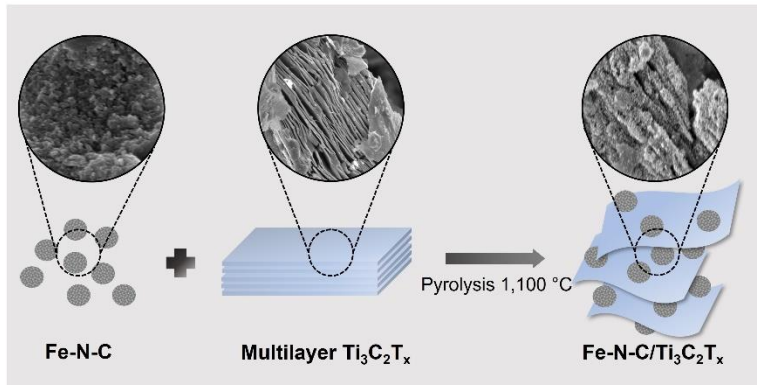
Abstract

The wide application of proton exchange membrane fuel cells (PEMFCs) is hindered by their slow oxygen reduction reaction (ORR) at the cathode. Therefore, to increase the practicality and economic viability of PEMFCs, non-noble metal catalysts have been developed to boost

the cathodic reaction. However, non-noble metal catalysts, such as Fe-N-C, typically exhibit lower activity than that of noble metal catalysts, which can reduce the efficiency of the fuel cell. In addition, non-noble metal catalysts suffer from durability issues that could degrade the catalyst over long-term operation. Therefore, in this study, we report the use of $\text{Ti}_3\text{C}_2\text{T}_x$ MXene as the catalyst support for a non-noble metal Fe-N-C catalyst for ORR. The unique layered structure of two-dimensional (2D) MXenes is beneficial as electrocatalysts owing to their high surface area, electrical conductivity and surface functionality. Fe-N-C was synthesized by doping Fe ions into a zeolitic imidazole framework (ZIF-8) precursor. Because of high-temperature treatment during the synthesis, MXene was introduced after the first pyrolysis with different mass ratios. A second pyrolysis heat treatment was further employed to optimize the catalyst activity and stability. This optimized new Fe-N-C/ $\text{Ti}_3\text{C}_2\text{T}_x$ -(4:1)-500 composite catalyst demonstrated higher ORR activity ($E_{\text{onset}} = 0.88$ V vs. RHE) than Fe-N-C ($E_{\text{onset}} = 0.83$ V vs. RHE) catalyst. Additionally, the stability of this Fe-N-C/ $\text{Ti}_3\text{C}_2\text{T}_x$ -(4:1)-500 found better than that of commercial Pt/C for over 10000 s based on a chronoamperometry test. More than 94% of the current remains after 10000 s for the composite catalyst, while Pt/C only retains 61% of the current. In addition, the use of $\text{Ti}_3\text{C}_2\text{T}_x$ MXene as the catalyst support for Fe-N-C improved the PEMFC performance. This work demonstrated that the hybridization of Fe-N-C and $\text{Ti}_3\text{C}_2\text{T}_x$ MXene shows great potential in constructing a high-performance low-cost fuel cell in the future.

Keywords: Stable catalyst, Fe-N-C, MXene, Oxygen reduction reaction, PEMFC

Graphical abstract



1 Introduction

Fuel cells are a clean and environmentally friendly technology for energy generation that produces electricity with less carbon footprint. This technology is driven by the hydrogen oxidation reaction (HOR) at the anode and the oxygen reduction reaction (ORR) at the cathode. Due to these reactions, fuel cells can produce electricity with only water as the by-product, making them a clean energy generation technology. However, the slow kinetics of the cathode reaction are limiting factors that hinder the application of fuel cells. The use of a Pt/C catalyst in both electrodes helps to boost the reactions, but this increases the total cost of the fuel cell. To overcome this issue, metal-nitrogen-carbon (M-N-C) catalysts have emerged as a type of catalyst material that could be used for the ORR. Among the M-N-Cs, Fe-N-C has received much attention due to its high catalytic activity [1,2]. In addition, the binding energy of O₂ on the Fe-N-C surface is not too strong and not too weak, which is advantageous for ORR [3]. As non-noble metal catalysts, Fe-N-Cs are typically designed to be as good as or better than Pt/C to achieve high activity and stability.

In recent years, metal-organic frameworks (MOFs) have emerged as promising precursors for Fe-N-C. MOFs are a type of porous material formed by arranging metal ions and organic molecules [4]. The unique features of MOFs, such as tuneable pore sizes, large surface areas, and the ability to selectively adsorb certain molecules, make them suitable precursors in the synthesis of M-N-C [4,5]. Additionally, MOFs can be easily functionalized to enhance their catalytic activity by introducing metal nanoparticles or functional groups on their surfaces. A remarkable ORR activity was obtained when MOFs were used in Fe-N-C. For example, Wang et al. demonstrated a high onset potential (E_{onset}) of 0.96 V vs. RHE in an alkaline media [6]. The Fe-based MOF used as the precursor created an Fe-N-C electrocatalyst embedded in an N-doped porous carbon framework, which improved the electrical

conductivity and increased the Fe-N active site exposure, allowing more rapid mass transfer and making it an excellent catalyst for the ORR. However, Fe-N-C catalysts are prone to corrosion and dissolution, especially in acidic electrolytes, leading to a loss in catalytic activity over time [7]. In addition, the Fe-N-C particles tend to aggregate during the operations of fuel cells, causing a decrease in the accessible active sites by the reactant. Therefore, many strategies have been employed to improve the activity and stability of the Fe-N-C catalyst, such as controlling the morphology [8,9], modifying the structural composition and adding catalyst support [10,11].

More than a decade ago, Gogotsi's group discovered a new material called MXene [12]. MXene consists of transition metal carbide, nitride or carbonitride with the chemical formula of $M_{n+1}X_nT_x$, in which M is transition metal, X is carbon or nitrogen or both and T_x is a surface termination group, such as -OH, -O or -F [13]. Due to the outstanding conductivity, high chemical stability, hydrophilicity and chemical robustness, more attention has been focused on utilizing MXenes in many applications, such as batteries [14-16], supercapacitors [17,18], water purification [19,20], technology in the medical field and many more [21,22]. Due to the combination of these properties, this material has also evolved as a catalyst support for electrocatalysts recently, especially for the application of ORR [23]. For instance, Xie et al. used $Ti_3C_2T_x$ MXene as the catalyst support for the first time to replace the conventional carbon support for Pt/C [24]. The electron transfer from the MXene support leads to the strong anchorage of Pt nanoparticles on the MXene, resulting in superior durability of the ORR catalyst of Pt/ $Ti_3C_2T_x$. On the other hand, MXenes have also been employed as non-noble electrocatalyst supports, as studied by other researchers [25,26]. For example, Xue et al. [27] introduced a Mn_3O_4 /MXene nanocomposite as the ORR catalyst for a zinc-air battery that generated a power density of 150 mW cm^{-2} , and Lin et al. [28] reported a hybrid Fe-Co-N-d- Ti_3C_2 catalyst that achieved a current density of 5.6 mA cm^{-2} in an alkaline electrolyte. These

studies show that this material is suitable as a catalyst support for ORR catalysts. In addition, a previous study also discovered that the coupling of FeN₄ with Ti₃C₂T_x possesses a strong interaction between these two materials, thus boosting the ORR [29].

??

Until now, research on the use of MXenes as catalyst supports for the ORR has not yet been expanded to fuel cell applications, especially PEMFCs. Most studies focused on ORR activity and durability, and very few investigate the performance of this material in fuel cells. The synergistic effect between Fe-N-C and Ti₃C₂T_x can lead to the improved performance of PEMFC, thus increasing its efficiency. Current ORR catalysts experience degradation during fuel cell operation, leading to decreased performance and shortened lifetimes. Therefore, exploring the ability of MXenes as catalyst support materials for the cathode of fuel cells is essential. Previously, a work by Jiang et al. discussed the use of metal clusters to adjust the surface charge of 2D nanosheets, in which iron-cluster-directed cationic Fe-N-C nanosheets were assembled with anionic MXene to produce a superlattice-like Fe-N-C/MXene heterostructure [26]. However, the work does not discuss the scalability of the synthetic procedure and its applicability to other types of metal clusters. In addition, a detailed analysis of the structural and chemical properties of the synthesized heterostructure was lacking, which could help to better understand the mechanism of the electrocatalytic activity. In a recent study by Gu et al., an efficient and stable electrocatalyst for ORR was synthesized using a combination of MOFs and Ti₃C₂ MXene [30]. The resulting Fe-N_x/N/Ti₃C₂ catalyst showed superior ORR performance in both acidic and alkaline environments. In this work, we introduce the use of multilayer Ti₃C₂T_x MXene as the catalyst support for zeolitic imidazole framework (ZIF-8)-derived Fe-N-C. Due to the high-temperature thermal treatment to synthesize ZIF-8-derived Fe-N-C and because MXene tends to decompose when treated at high temperature, we separately added the MXene support after the synthesis of Fe-N-C. After adding the MXene

support, a second-step pyrolysis was performed in this work, which resulted in a significant improvement in the stability of the Fe-N-C/Ti₃C₂T_x MXene. The Fe-N-C and Ti₃C₂T_x MXene showed strong interactions through bond formation between Ti and N upon second-step pyrolysis, which significantly improved the ORR activity and stability, thus improving the power density in PEMFCs. The development of this new ORR catalyst shows a great potential of non-noble metal cathode catalyst for the ORR in fuel cells, helping expand the applications of sustainable fuel cells in the future.

2 Experimental

2.1 Materials

Multilayer MXenes (Ti₃C₂T_x, 68%) were purchased from ACS Material. Zinc (II) nitrate hexahydrate (Zn(NO₃)₂·6H₂O, AR) and iron nitrate hexahydrate (Fe(NO₃)₃·9H₂O, AR) were obtained from R&M Chemicals, 2-methylimidazole (99%) was purchased from Sigma Aldrich, dimethylformamide (DMF) was purchased from Fisher Scientific, and methanol (AR) and ethanol (AR) were obtained from HmBG. All chemicals were used without further purification.

2.2 Synthesis of Fe-N-C

Zinc nitrate hexahydrate, iron nitrate nonahydrate and 2-methylimidazole were mixed in 600 ml methanol solution at a fixed molar ratio of 1:0.025:4.21 and stirred for 24 h at 60 °C. Next, the precipitate was washed with ethanol and dried in a vacuum oven at 60 °C overnight. Finally, the samples underwent heat treatment at 1,100 °C for 1 h under N₂ flow with a ramping rate of 5 °C/min.

2.3 Synthesis of Fe-N-C/Ti₃C₂T_x

To synthesize Fe-N-C/MXene, Fe-N-C and Ti₃C₂T_x MXene were mixed in 50 ml dimethylformamide (DMF) solution at different mass ratios of 1:1, 2:1, 4:1, 6:1 and 8:1 to

achieve a colloidal suspension of 1 mg ml^{-1} . The mixture was then sonicated for 6 hours using bath sonication to ensure the deposition of Fe-N-C on the $\text{Ti}_3\text{C}_2\text{T}_x$ MXene. After that, the precipitate was washed with deionized water using the centrifugal method and dried in a vacuum oven at $60 \text{ }^\circ\text{C}$ overnight. The samples were collected and labelled as Fe-N-C/ $\text{Ti}_3\text{C}_2\text{T}_x$ - (mass ratio). For example, Fe-N-C/ $\text{Ti}_3\text{C}_2\text{T}_x$ -(4:1) indicates that a mass ratio of 4:1 was used for that sample. To investigate the effect of the second pyrolysis, the best mass ratio of Fe-N-C/ $\text{Ti}_3\text{C}_2\text{T}_x$ was further pyrolyzed at $350 \text{ }^\circ\text{C}$, $500 \text{ }^\circ\text{C}$ and $800 \text{ }^\circ\text{C}$ for 1 h under N_2 flow (ramping rate: $5 \text{ }^\circ\text{C/min}$).

2.4 Material characterization

Physicochemical characterization was conducted to obtain the physical and chemical properties of the catalyst. Structure and morphology studies were carried out using field emission scanning electron microscopy (GeminiSEM 500) and transmission electron microscopy (FEI Talos L120C). The crystallographic structures were recorded using X-ray diffraction (PANalytical X'Pert PRO) and analysed using HighScore Plus software. Nitrogen adsorption-desorption was carried out using a Micromeritics 3Flex Analyser at 77 K for surface area and porosity characterization. Prior to measurement, the samples were degassed at $150 \text{ }^\circ\text{C}$ for 8 hours to remove any adsorbed gases or moisture. The Brunauer-Emmett-Teller (BET) method was used to calculate the surface area of the sample, while the Barret-Joyner-Halenda (BJH) method was used to determine the pore size distribution of the sample. The chemical bonding and composition of the catalyst were measured using X-ray photoelectron spectroscopy (XPS) (Kratos Axis Ultra) with Al Monochromatic. The XPS spectra were further analysed using CASA XPS software for deconvolution and peak fitting.

2.5 Electrochemical measurement

A three-electrode cell was used for the electrochemical measurement, which was carried out in 0.1 M HClO_4 electrolyte. The measurement was conducted on an Autolab PGSTAT128N

potentiostat with platinum foil as the counter electrode and Ag/AgCl as the reference electrode. Before the measurement, the catalyst was prepared in ink form by dispersing in ethanol and 10 wt. % Nafion solution, followed by sonication for 30 mins to obtain a homogenous ink suspension. A 5 mm diameter glassy carbon with a platinum ring was used as the working electrode. Prior to the deposition of the catalyst on the working electrode, the glassy carbon was polished with a 0.05 μm alumina slurry until a mirror-like surface was obtained. Then, 10 μl of the catalyst was dropped on the electrode surface and dried under atmospheric conditions before the measurement was obtained.

Cyclic voltammetry (CV) and linear sweep voltammetry (LSV) were conducted at scan rates of 50 mV s^{-1} and 10 mV s^{-1} , respectively, in both N_2 - and O_2 -saturated electrolytes at room temperature. For LSV, the current readings were background corrected by subtracting the non-faradaic capacitance current density. All potential readings were converted to a reversible hydrogen electrode (RHE) as reported by others [31]. The rotating ring-disk electrode (RRDE) technique was used for the electrochemical measurement. The electron transfer number (n) and the percentage of $-\text{OOH}^-$ produced ($\% -\text{OOH}^-$) were calculated using Equation 1 and Equation 2, respectively.

$$n = (4I_d)/(I_d + (\frac{I_r}{N})) \quad (2)$$

$$\text{HO}_2^- \% = ((4 - n)/2) \times 100 \quad (3)$$

where I_d , I_r , and N are the disk current, ring current and collection efficiency, respectively.

2.6 MEA fabrication and single-cell testing

The catalyst ink was prepared by mixing the catalyst with isopropyl alcohol and Nafion solutions. The catalyst was deposited on gas diffusion layer carbon paper (AvCarb GDS3250) using the spraying method to obtain a loading of 4 mg/cm^2 at the cathode. At the anode, a gas

diffusion electrode with 0.5 mg/cm^2 60 wt.% Pt/C was used. Prior to testing, Nafion[®] 212, as the proton exchange membrane, was sandwiched between the two electrodes and hot-pressed at $120 \text{ }^\circ\text{C}$ with a pressure of 30 bar for 3 minutes to obtain the membrane-electrode-assembly (MEA) with an active area of 6.25 cm^2 . The single-cell performance was evaluated at room temperature with 100% relative humidity. 0.08 L/min of H_2 gas was fed as the fuel at the anode, and 0.2 L/min of O_2 as the oxidant at the cathode for the PEMFC. The single-cell performance measurements were recorded using Fuel Cell Monitor 4.0.

?

3 Results and discussion

3.1 Effect of mass ratio

Fig. 1 illustrates the synthesis process of Fe-N-C/ $\text{Ti}_3\text{C}_2\text{T}_x$. Fe-N-C was obtained by doping Fe ions into the zeolite imidazole framework (ZIF-8) precursor. Through the subsequent heat treatment at $1100 \text{ }^\circ\text{C}$, the Zn ions on the precursor are removed, thus providing a highly porous Fe-N-C particle. This high-temperature pyrolysis is important to convert the Fe-N₄ complexes into FeN₄ active sites embedded in the carbon matrix [32]. During the pyrolysis process, the Fe ions within the Fe-doped ZIF-8 decompose and react with the carbon and nitrogen in the ZIF-8 framework to form Fe-N-C sites. The high-temperature treatment also induces the removal of the ZIF-8 template, leaving behind a porous carbon matrix that provides a high surface area for electrochemical reactions. In particular, the high-temperature treatment at $1100 \text{ }^\circ\text{C}$ leads to the formation of highly active Fe-N-C sites, which play a critical role in enhancing the ORR performance of the catalyst. Further addition of the $\text{Ti}_3\text{C}_2\text{T}_x$ MXene support led to the deposition of Fe-N-C particles on the $\text{Ti}_3\text{C}_2\text{T}_x$ MXene surface, followed by a second pyrolysis to enhance the interaction between Fe-N-C and $\text{Ti}_3\text{C}_2\text{T}_x$ MXene.

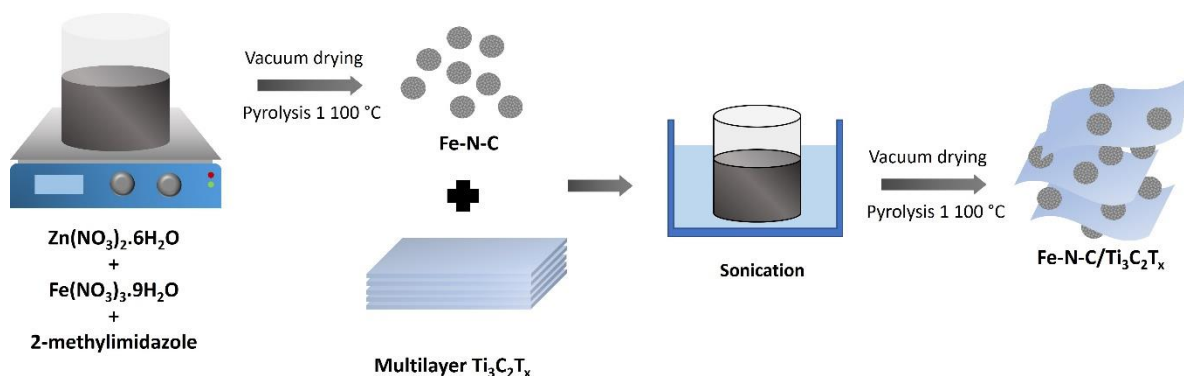


Fig. 1. Schematic synthesis route of Fe-N-C/ $\text{Ti}_3\text{C}_2\text{T}_x$.

As shown in the FESEM image displayed in Fig. 2a-f, when Fe-N-C and MXene are mixed at a 1:1 mass ratio, the Fe-N-C catalyst particles are observed to deposit on the surface of the MXene layers. This is likely due to the strong interaction between the Fe-N-C particles and the MXene surface, which is rich in functional groups such as -OH and -O. These functional groups can act as anchor points for the Fe-N-C particles, causing them to adhere to the surface of the MXene layers [33]. As the mass ratio of Fe-N-C to MXene is increased to 8:1, the Fe-N-C particles begin to occupy the interlayer spaces between the MXene layers, forming a more compact and dense structure. Fig. 2g shows the XRD spectra of the synthesized Fe-N-C/ $\text{Ti}_3\text{C}_2\text{T}_x$. The XRD spectra of Fe-N-C display the presence of a prominent (002) graphitic carbon peak at $2\theta = 26^\circ$ [31], with small peaks at $2\theta = 29.74^\circ$ and 43.43° corresponding to the (101) and (111) planes of Fe_3N according to JCPDS card no. 49-1664 [34]. Additionally, the small peaks at 35° , 44° , 57.5° , and 62.5° are attributed to the (311), (400), (511) and (440) planes of Fe_2O_3 (JCPDS card no. 39-1346). The pristine multilayer $\text{Ti}_3\text{C}_2\text{T}_x$ shows prominent peaks at 8.9° , 18.6° , 37.7° and 60.7° , which correspond to the (002), (006), (0012) and (110) planes, indicating a multilayer $\text{Ti}_3\text{C}_2\text{T}_x$ MXene [26]. The (002) peaks of $\text{Ti}_3\text{C}_2\text{T}_x$ MXene gradually broaden and shorten as Fe-N-C is added, suggesting an increase in the d-spacing of the $\text{Ti}_3\text{C}_2\text{T}_x$ layers due to the incorporation of Fe-N-C into the MXene sheets [35].

The ORR activity of these catalysts was tested in 0.1 M HClO₄ electrolyte, simulating the operating conditions of the acidic environment of PEMFCs. Fig. 2h shows that the addition of Ti₃C₂T_x MXene reduces the current density with only a small drop in the onset potential. This is because MXene has poor ORR catalytic activity due to its inert nature and lack of active sites for ORR. It was observed that the highest onset potential was produced by Fe-N-C/Ti₃C₂T_x-(4:1), with an E_{onset} of 0.8 V vs. RHE. There is no linear correlation between the mass ratio used for the preparation of Fe-N-C/Ti₃C₂T_x and the ORR activity. In fact, adding an inadequate amount of MXene did not improve the ORR activity, yet excessive MXene led to a decrease in ORR activity. Therefore, the optimal mass ratio of Fe-N-C/Ti₃C₂T_x at 4:1 was selected and set for further testing.

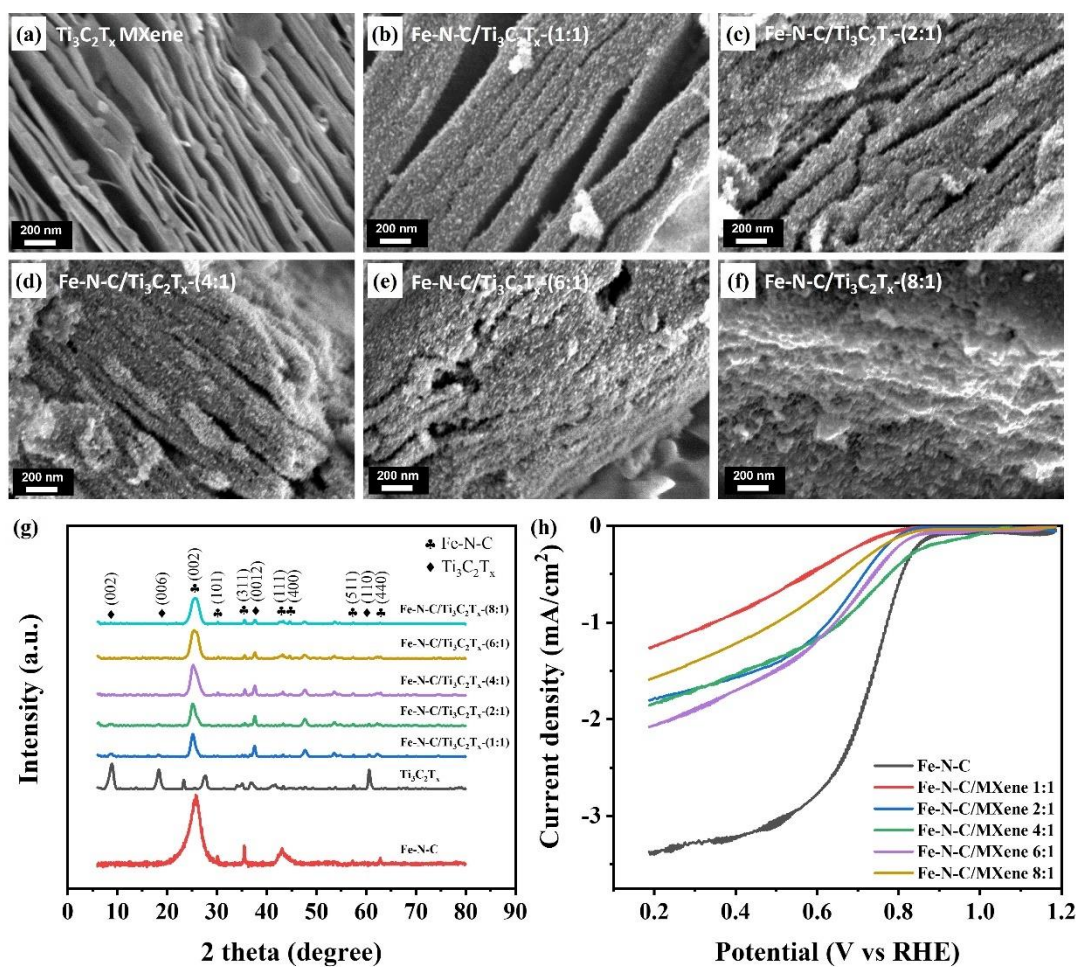


Fig. 2. (a-f) FESEM image, (g) XRD spectra and (h) linear sweep voltammetry of Fe-N-C, Ti₃C₂T_x, Fe-N-C/Ti₃C₂T_x-(1:1), Fe-N-C/Ti₃C₂T_x-(2:1), Fe-N-C/Ti₃C₂T_x-(4:1), Fe-N-C/Ti₃C₂T_x-(6:1) and Fe-N-C/Ti₃C₂T_x-(8:1).

3.2 Effect of pyrolysis temperature

To further improve the catalytic activity of Fe-N-C/Ti₃C₂T_x, a second pyrolysis step was added. In the first pyrolysis step during the synthesis of Fe-N-C, precursor materials, such as Fe and N-containing carbon matrices, are converted into a carbon-based material with a disordered and amorphous structure. Therefore, the second pyrolysis post-addition of Ti₃C₂T_x MXene is vital. This step helps to improve the crystal structure and increase the degree of graphitization of the carbon material. This improves the conductivity and exposes more active sites for the ORR reaction, leading to an enhancement in catalytic activity. The degree of

graphitization of the catalyst can have a significant impact on the stability of the catalyst. In general, a highly graphitized catalyst typically exhibits higher stability and durability, as the highly ordered graphitic structure is more resistant to corrosion and degradation during the operation of the fuel cell [36]. The FESEM micrographs depicted in Fig. 3a-d reveal the presence of Fe-N-C particles deposited on the surface of $\text{Ti}_3\text{C}_2\text{T}_x$ MXene. Interestingly, as a second pyrolysis is imposed, the MXene introduced a gap between the layers. In addition, the lateral size of MXene is reduced. This is favourable because it could increase the surface area and provide a pathway for mass transport of a reactant. As the pyrolysis temperature was further increased to 800 °C, the structure of MXene began to decompose, resulting in the formation of larger particles. The TEM image presented in Fig. 3e-h demonstrated that the hollow sphere structure of Fe-N-C was still visible on the surface of $\text{Ti}_3\text{C}_2\text{T}_x$ MXene, yet no such structure was observed in Fe-N-C/ $\text{Ti}_3\text{C}_2\text{T}_x$ -(4:1)-800.

It is assumed that at 800 °C, the $\text{Ti}_3\text{C}_2\text{T}_x$ surface was oxidized and formed TiO_2 . From the XRD spectra presented in Fig. 3i, Fe-N-C/ $\text{Ti}_3\text{C}_2\text{T}_x$ -(4:1)-350 and Fe-N-C/ $\text{Ti}_3\text{C}_2\text{T}_x$ -(4:1)-500 show similar XRD patterns to Fe-N-C/ $\text{Ti}_3\text{C}_2\text{T}_x$ -(4:1). However, further increasing the second pyrolysis temperature to 800 °C leads to the formation of TiO_2 on the $\text{Ti}_3\text{C}_2\text{T}_x$ surface, as shown by the sharp peak at 27.3° that matched the rutile TiO_2 (110) plane (JCPDS #75-1537) [37].

In Fig. 3j, the N_2 adsorption-desorption of pristine $\text{Ti}_3\text{C}_2\text{T}_x$ presented a type III isotherm that defined the nonporous structure of the multilayer $\text{Ti}_3\text{C}_2\text{T}_x$. On the other hand, Fe-N-C/ $\text{Ti}_3\text{C}_2\text{T}_x$ -(4:1)-500 generates a type IV isotherm with hysteresis H3, which illustrates a mesopore structure [38]. The steep increase in $P/P_0 < 0.05$ for Fe-N-C, Fe-N-C/ $\text{Ti}_3\text{C}_2\text{T}_x$ -(4:1) and Fe-N-C/ $\text{Ti}_3\text{C}_2\text{T}_x$ -(4:1)-500 indicates the presence of micropores in these catalysts [39]. The BET surface areas calculated based on the N_2 adsorption-desorption isotherms for $\text{Ti}_3\text{C}_2\text{T}_x$, Fe-N-C, Fe-N-C/ $\text{Ti}_3\text{C}_2\text{T}_x$ -(4:1) and Fe-N-C/ $\text{Ti}_3\text{C}_2\text{T}_x$ -(4:1)-500 are 1.53, 492.7, 222.8 and 359.8

m^2/g , respectively. The increase in the surface area of Fe-N-C/Ti₃C₂T_x-(4:1)-500 is due to the increase in the interplanar distance post-second pyrolysis [40]. In addition, the pyrolysis of Fe-N-C/Ti₃C₂T_x-(4:1)-500 leads to the formation of defects and mesopores, thus increasing the surface area [41]. The pore size distribution (Fig. 3k) shows that Fe-N-C/Ti₃C₂T_x-(4:1)-500 contains fewer macropores than Fe-N-C/Ti₃C₂T_x-(4:1) with no pyrolysis. This is because the high temperature during pyrolysis can cause the Ti₃C₂T_x MXene layers to partially collapse and fuse together, leading to a decrease in the number of interlayer spaces and ultimately reducing the number of macropores in the material.

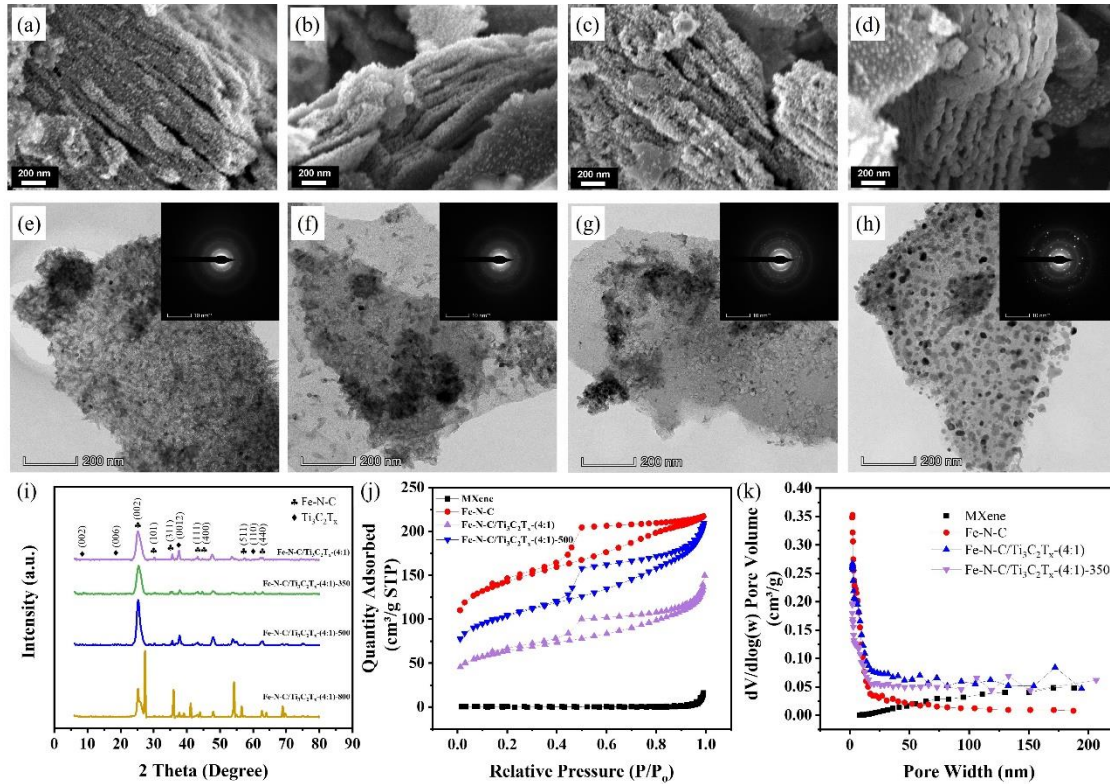


Fig. 3. FESEM image of (a) Fe-N-C/Ti₃C₂T_x-(4:1), (b) Fe-N-C/Ti₃C₂T_x-(4:1)-350, (c) Fe-N-C/Ti₃C₂T_x-(4:1)-500 and (d) Fe-N-C/Ti₃C₂T_x-(4:1)-800. TEM image of (e) Fe-N-C/Ti₃C₂T_x-(4:1), (f) Fe-N-C/Ti₃C₂T_x-(4:1)-350, (g) Fe-N-C/Ti₃C₂T_x-(4:1)-500 and (h) Fe-N-C/Ti₃C₂T_x-(4:1)-800. (i) XRD spectra of Fe-N-C/Ti₃C₂T_x-(4:1) with different pyrolysis temperatures. (j) N₂ adsorption-desorption isotherm and (k) pore size distribution of MXene, Fe-N-C, Fe-N-C/Ti₃C₂T_x-(4:1) and Fe-N-C/Ti₃C₂T_x-(4:1)-500.

XPS measurements were carried out to obtain information on the composition and chemical state of Fe-N-C/Ti₃C₂T_x. The XPS survey scan in Fig. 4a reveals that Fe-N-C mainly contains Fe, O, N and C species, while the addition of Ti₃C₂T_x MXene shows the presence of Ti and F species on Fe-N-C/Ti₃C₂T_x. This indicates that the Ti₃C₂T_x MXene contains -F and -OH groups on the surface termination. Additionally, it is observed that the amount of Fe present in the samples is extremely low, possibly due to the formation of single atoms. The N peaks in the XPS spectrum were analysed and deconvoluted into four distinct types of N bonding, as shown in Fig. 4b-d. The quantitative measurement of the N species present in the samples is summarized in the bar chart in Fig. 4e. The second pyrolysis of Fe-N-C/Ti₃C₂T_x leads to an increase in pyridinic-N and graphitic-N. This is beneficial for the ORR, as pyridinic-N is known to play an important role in the ORR because it can act as an active site for the reaction [42]. The abundant existence of micropores and pyridinic N, which are predominantly situated at the edges and defects of the carbon matrix, indicates that nitrogen-doped microporous defects are prevalent. These pre-existing N-C defects are believed to act as anchoring sites, facilitating the formation of SA FeN_x sites [43].

The presence of Ti₃C₂T_x MXene nanosheets can influence the bonding of Ti and N in the Fe-N-C/MXene material. The Ti atoms in the MXene nanosheets can interact with the N atoms in the Fe-N-C nanoparticles, leading to the formation of Ti-N bonds. These Ti-N bonds can potentially influence the electronic structure and catalytic properties of the Fe-N-C nanoparticles. The XPS Ti 2p peak was further deconvoluted into four peaks, which were identified as TiO₂ and TiN, as shown in Fig. 4f-g. Interestingly, the atomic percentage of TiN is increased after the second pyrolysis from 6.29 at. % to 17.75 at. %.

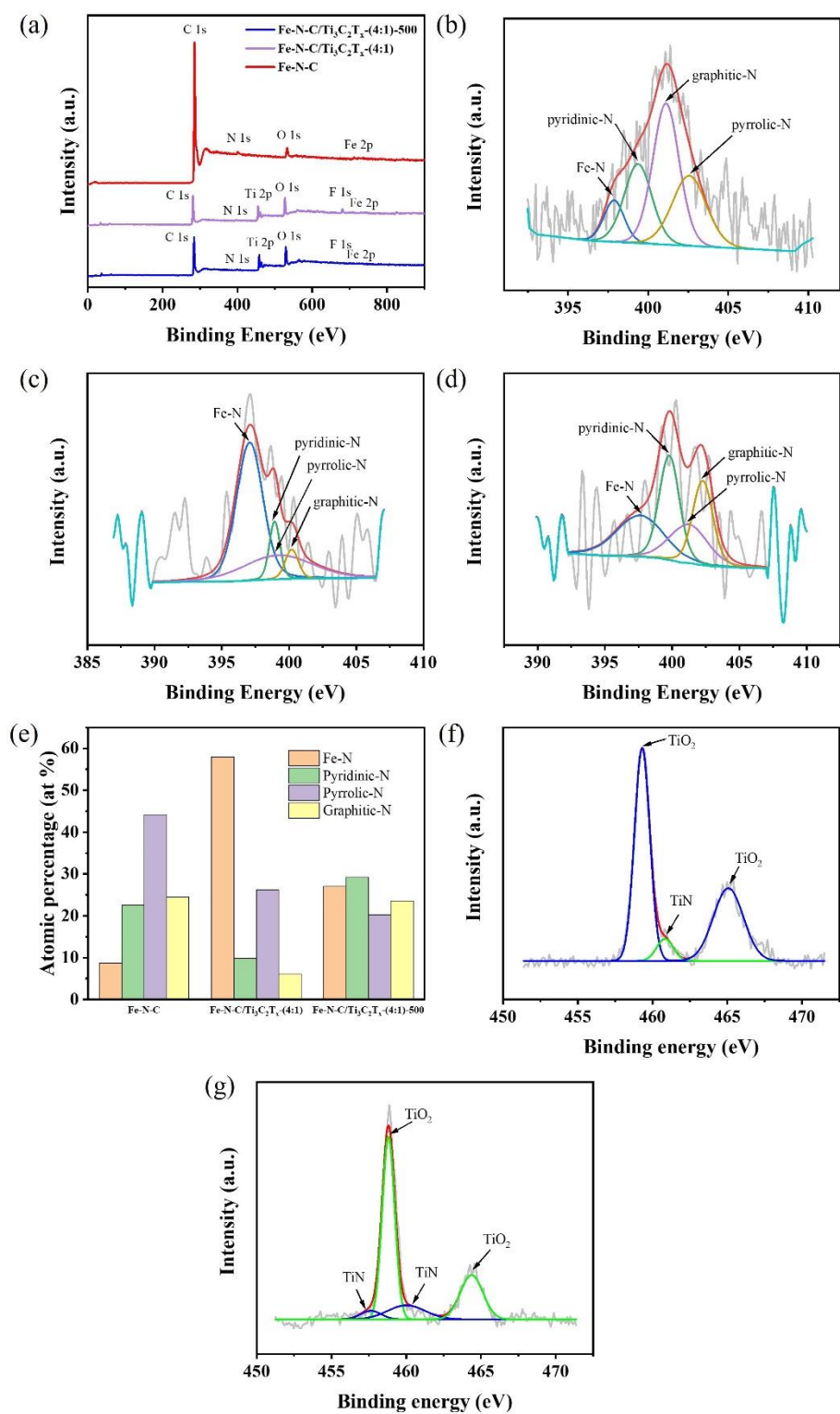


Fig. 4. (a) XPS survey spectra. High-resolution spectra of N1s for (b) Fe-N-C, (c) Fe-N-C/Ti₃C₂T_x-(4:1) and (d) Fe-N-C/Ti₃C₂T_x-(4:1)-500. (e) The percentage of N species in N 1s. High-resolution spectra of Ti2p for (f) Fe-N-C/Ti₃C₂T_x-(4:1) and (g) Fe-N-C/Ti₃C₂T_x-(4:1)-500.

The electrocatalytic activity of the Fe-N-C/MXene catalysts was tested in 0.1 M HClO₄ electrolytes. As shown in Fig. 5a, there is a significant enhancement in the ORR activity when Fe-N-C/Ti₃C₂T_x-(4:1) undergoes a second pyrolysis. No change in E_{onset} was observed with the second pyrolysis, yet the limiting current density is increased. The Fe-N-C/Ti₃C₂T_x-(4:1)-500 exhibited a higher current density of 3.6 mA/cm² compared to that of the Fe-N-C/Ti₃C₂T_x-(4:1) with no second pyrolysis (1.38 mA/cm²). This indicates that 500 °C is the best pyrolysis temperature for Fe-N-C/Ti₃C₂T_x. Further microkinetic studies were conducted by calculating the Tafel slope obtained from the kinetic region. As seen in Fig. 5b, Fe-N-C/Ti₃C₂T_x-(4:1)-500 has the lowest Tafel slope (100 mV/dec), much lower than that of Fe-N-C/Ti₃C₂T_x-(4:1) without further second pyrolysis and Fe-N-C. This indicates that Fe-N-C/Ti₃C₂T_x-(4:1)-500 possesses the fastest electron transfer rate for ORR compared to that of the other samples. The electron transfer number for the samples was further calculated using the RRDE method. As observed in Fig. 5c, all Fe-N-C/Ti₃C₂T_x-(4:1) with and without further pyrolysis possess an electron transfer number greater than 3.85, which indicates the 4-electron transfer. However, the highest electron transfer number is acquired by Fe-N-C/Ti₃C₂T_x-(4:1)-500 with 3.97. The unique nanostructure of the catalyst, with its porous properties, provides more accessible catalytic sites and enhances the transportation of reactants, which is critical for the ORR process. Additionally, this Fe-N-C/Ti₃C₂T_x-(4:1)-500 produced the lowest hydrogen peroxide, which was less than 3%.

The electronic structure changes of FeN₄ after coupling with Ti₃C₂T_x greatly affects the ORR. Ti₃C₂T_x MXene, which contains -OH and -F terminations with high electronegativity, can strongly interact with FeN₄ moieties and stabilize the highest occupied molecular orbital (HOMO) by reducing the electron density of Fe(II). This decreased electron density around Fe(II) centres, combined with strong electron delocalization, optimizes the orbital overlap of

Fe 3d with O₂ 2p and favours the jump of Fe d_{z²} electron to O 2p orbitals, thus boosting oxygen adsorption on FeN₄ [29]. The position of the d-band centre is a main factor that determines the adsorption strength of the intermediates. As a consequence, more d electrons are introduced to the d unoccupied orbitals, which makes the d-band centre move away from the Fermi level and therefore weakens the binding strength of O species; as a result, the ORR activity is boosted [24,44].

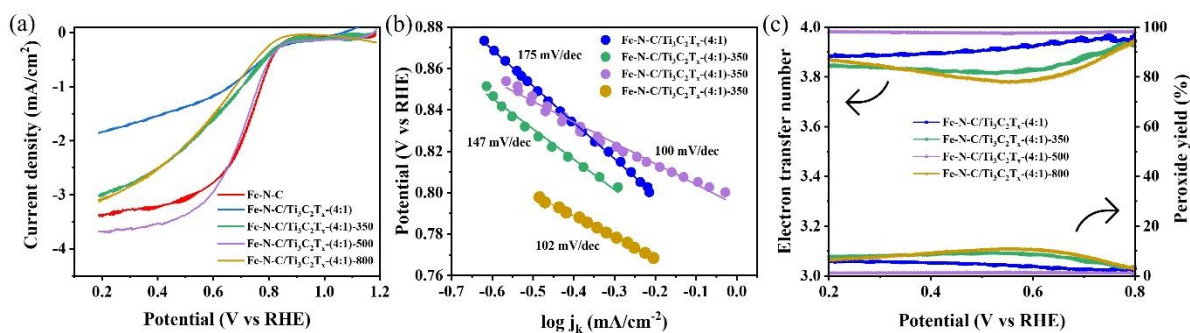


Fig. 5. (a) Linear sweep voltammetry of Fe-N-C and Fe-N-C/Ti₃C₂T_x-(4:1) with pyrolysis temperatures of 350, 500 and 800 °C, (b) Tafel plot and (c) electron transfer number and peroxide yield for Fe-N-C/Ti₃C₂T_x-(4:1), Fe-N-C/Ti₃C₂T_x-(4:1)-350, Fe-N-C/Ti₃C₂T_x-(4:1)-500 and Fe-N-C/Ti₃C₂T_x-(4:1)-800

The main factors that lead to the degradation of catalysts and result in a decline in performance are the leaching of metals, corrosion of carbon, production of hydrogen peroxide, and protonation of active sites. These factors could affect the catalyst's durability, especially when applied in the fuel cell environment. Therefore, the durability of the catalyst was tested using an accelerated durability test (ADT) by applying a load cycle in the potential range of 0.6 to 1.0 V vs. RHE in N₂-saturated 0.1 M HClO₄, following the standard ADT protocol [25,45,46]. CV and LSV were recorded pre- and post-ADT (Fig. 6). The initial E_{1/2} for Fe-N-C/Ti₃C₂T_x-(4:1) was 0.686 V vs. RHE and dropped to 0.641 V vs. RHE, indicating a 45 mV loss. Meanwhile, Fe-N-C/Ti₃C₂T_x-(4:1)-500 only lost 7 mV of E_{1/2} after the ADT. This

demonstrates that Fe-N-C/Ti₃C₂T_x-(4:1)-500 is more durable than Fe-N-C/Ti₃C₂T_x-(4:1) in a harsh ADT environment.

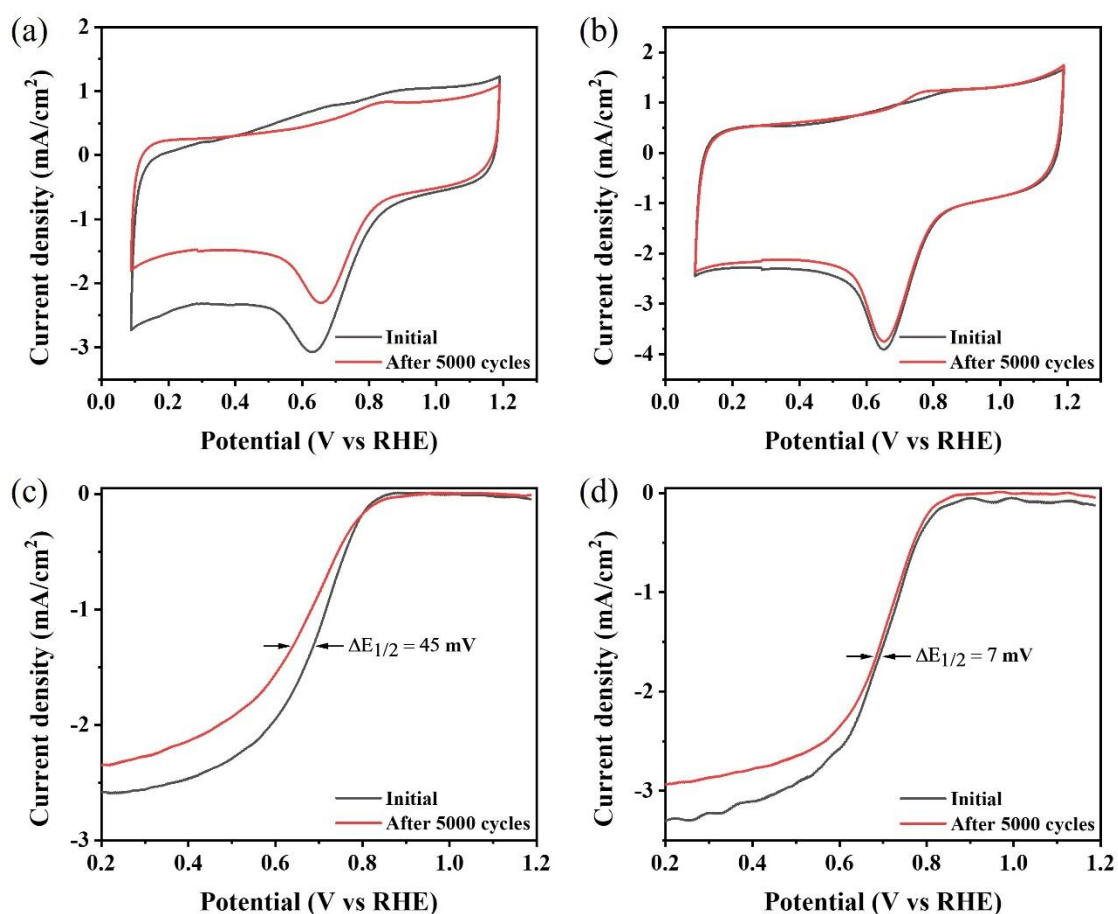


Fig. 6. CV of (a) Fe-N-C/Ti₃C₂T_x-(4:1) and (b) Fe-N-C/Ti₃C₂T_x-(4:1)-500, and LSV of (c) Fe-N-C/Ti₃C₂T_x-(4:1) and (d) Fe-N-C/Ti₃C₂T_x-(4:1)-500 before and after the 5,000 cycles of ADT.

Continuous chronoamperometry measurements were carried out to investigate the stability of the catalyst. The current-time curve was obtained by performing the chronoamperometry test at 0.6 V for 10,000 s in an O₂-environment electrolyte. As shown in Fig. 7, Fe-N-C/Ti₃C₂T_x-(4:1)-500 exhibits the most current stability, with 94% of the current remaining over 10000 s. In contrast, the commercial Pt/C catalyst exhibits a lower stability, retaining only 61% of the current, as previously reported by another study [47]. The notable

decrease in current observed during the chronoamperometry test for Pt/C was primarily attributed to carbon corrosion and Pt dissolution, which were especially prominent in an acidic environment [48]. The formation of H_2O_2 during the ORR can have a significant impact on the stability of the catalyst. H_2O_2 is a reactive oxygen species that can react with the catalyst surface, leading to degradation of the catalyst and a decrease in its activity. The presence of H_2O_2 can also lead to the formation of free radicals, which can further damage the catalyst surface and reduce its stability [49]. This can be attributed to the lowest H_2O_2 production during the ORR on the Fe-N-C/Ti₃C₂T_x-(4:1)-500 catalyst. One reason why MXenes are stable ORR catalysts is their unique structure and composition. MXenes have a layered structure that consists of transition metal layers (such as Ti, Mo, V, etc.) sandwiched between carbon or nitrogen layers [50]. These layers are held together by strong metallic bonds, giving MXenes their mechanical strength and stability [51]. In addition, the graphitized carbon layers were found to be advantageous in maintaining the stability of the current by preventing the aggregation and dissolution of Fe [52]. The interaction between Ti and Fe-N-C can improve the stability due to the strong bonding between Ti and Fe-N-C that can prevent the leaching of Fe or other active species from the catalyst, which is a common issue with ORR catalysts. In addition, this interaction leads to the transfer of electrons at the interface and atomic charge polarization between the two layers [34].

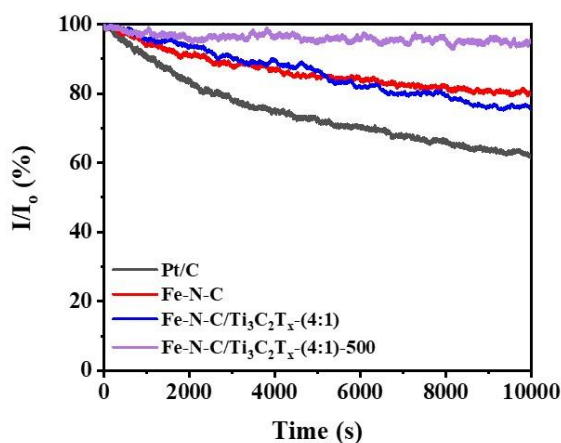


Fig. 7. Current-time (i-t) chronoamperometric responses for the ORR of Fe-N-C, Fe-N-C/Ti₃C₂T_x-(4:1), Fe-N-C/Ti₃C₂T_x-(4:1)-500 and Pt/C.

Various modifications have been investigated by other researchers to enhance the activity and stability of Fe-N-C catalysts for ORR in fuel cells. These modifications include adding other transition metals, such as cobalt, nickel, or manganese, to the Fe-N-C catalyst, which can provide more active sites and improve electron transfer rates. Another strategy involves functionalizing the catalyst surface with nitrogen-containing groups or graphene to enhance its durability and activity. Additionally, optimizing precursor and synthesis conditions can improve the distribution and composition of active sites. These modifications have the potential to make Fe-N-C catalysts an attractive choice for fuel cells and other electrochemical applications. Table 1 summarizes the works performed by other researchers to improve the performance of Fe-N-C catalysts, especially in terms of catalyst stability.

Table 1 Comparison of various Fe-N-C samples and their performance as ORR catalysts in 0.1 M HClO₄ from other studies.

Catalyst	E _{onset} (V vs. RHE)	E _{1/2} (V vs. RHE)	ORR stability	Ref.
Fe-N-C/Ti ₃ C ₂ T _x - (4:1)-500	0.88	0.68	Retained 94% of current over 10,000s chronoamperometry test and only 7 mV of E _{1/2} attenuation after the 5000 cycles ADT	This work
Fe-N-C@MXene		0.77	11 mV of E _{1/2} attenuation after the 10000 cycles ADT	[53]
Cu-Fe-N-C	0.90	0.79	20 mV of E _{1/2} attenuation after the 1000 cycles ADT	[54]
Pt-FeNC	0.97	0.85	20 mV of E _{1/2} attenuation after the 10000 cycles ADT	[55]
S-doped Fe-N-C	0.95	0.81	2 mV of E _{1/2} attenuation after the 10000 cycles ADT	[56]
FeMn-N-C	0.989	0.804	Retained 96% of current over 40,000s chronoamperometry test	[57]
FeNSF-doped C	0.901	0.798	24.8 mV of E _{1/2} attenuation after the 10000 cycles ADT	[58]
FeNi-N-C	0.90	0.79	No attenuation of E _{1/2} after the 5000 cycles ADT	[59]

FeCr-N-C	0.88	0.73	14 mV of $E_{1/2}$ attenuation after the 20000 cycles ADT	[60]
Fe-N-C-900	0.841	0.709	33 mV of $E_{1/2}$ attenuation after the 5000 cycles ADT	[61]
P-doped Fe-N-C	0.92	0.858	N/A	[62]

3.3 Performance of single-cell PEMFC

The performance of the Fe-N-C/Ti₃C₂T_x MXene was further evaluated in a single-cell PEMFC at room temperature. Considering its excellent catalytic activity as revealed by its ORR activity, kinetic parameters and stability, Fe-N-C/Ti₃C₂T_x-(4:1)-500 was selected to be tested in a single-cell PEMFC. The I-V polarization curve and power density profile of the catalyst are presented in Fig. 8. At room temperature, Fe-N-C/Ti₃C₂T_x-(4:1)-500 achieves a maximum power density of 18.3 mW/cm², which is higher than that of Fe-N-C (only 8.1 mW/cm²). This is because the synergistic effect between Fe-N-C and Ti₃C₂T_x MXene promotes the reaction rate and thus improves the power density of the PEMFC. However, it was observed that the open circuit voltage (OCV) of Fe-N-C/Ti₃C₂T_x-(4:1)-500 is lower (0.67 V) than that of the Fe-N-C (0.7 V). However, in the ohmic region, the current for Fe-N-C/Ti₃C₂T_x-(4:1)-500 surpasses that for Fe-N-C, thus producing a higher power density. This is because the high electrical conductivity of Ti₃C₂T_x MXene can facilitate the electron transfer process, reducing the resistance of the catalyst layer and improving the overall performance of the PEMFC [63]. Therefore, the addition of Ti₃C₂T_x MXene into Fe-N-C can improve the overall performance of the PEMFC, leading to an increase in power density. However, despite their improved performance, the Fe-N-C/Ti₃C₂T_x-(4:1)-500 catalysts still exhibit lower single-cell performance than that of Pt/C. From this experimental, the performance of Pt/C is lower than

that reported elsewhere [64], however, when the hot-press condition during the MEA fabrication is changed to a lower pressure, the power density of the Pt/C electrode increases significantly to 153.2 mW/cm². This observation suggests that the hot-press condition has a significant impact on the performance of the fuel cell. In the future, it is expected that further advancements in optimizing the MEA preparation and hot-pressing techniques will lead to even higher performance and efficiency of PEMFCs using noble-free metal catalysts.

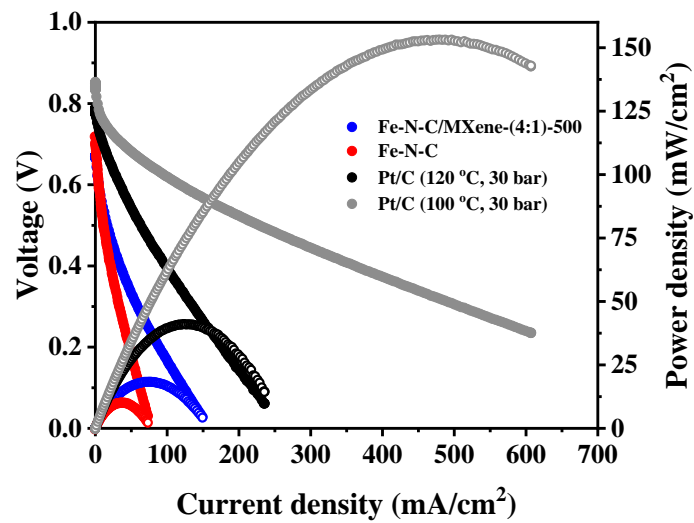


Fig. 8. Single cell PEMFC of Fe-N-C and Fe-N-C/ Ti₃C₂T_x-(4:1)-500 at room temperature in comparison to Pt/C (cathode loading of 0.5 mg/cm²) with the same MEA preparation method and different hot-press conditions.

4 Conclusion

In conclusion, this study has demonstrated that Fe-N-C/Ti₃C₂T_x MXene is a promising catalyst for ORR due to its excellent catalytic activity and durability. Our results indicate that the addition of MXene on Fe-N-C with two-step pyrolysis at the optimum temperature could improve the ORR activity, with a high onset potential and exceptional durability. Additionally, this Fe-N-C/Ti₃C₂T_x MXene catalyst shows excellent stability under prolonged testing with 1.5-fold of the current remaining in Pt/C, suggesting that it shows the potential for long-term

applications in fuel cells and other electrochemical devices. The synergistic effect between Fe-N-C and MXene occurs due to the complementary properties of these two materials. Fe-N-C exhibits excellent catalytic activity for the ORR but suffers from poor durability due to carbon corrosion. On the other hand, MXene shows good stability but exhibits poor ORR activity. By combining Fe-N-C and MXene, the advantages of both materials can be exploited while minimizing their drawbacks. The MXene serves as a support for Fe-N-C, improving its durability by providing a protective layer against carbon corrosion. At the same time, Fe-N-C enhances the ORR activity of MXene by providing active sites for the reaction. This work provides clear insight into the highly active and stable Fe-N-C/Ti₃C₂T_x towards ORR and its performance in PEMFC. The development of this new ORR catalyst could provide an opportunity to further expand sustainable fuel cell applications in the future.

?

Acknowledgement

This project was financially supported by the Ministry of Higher Education (MOHE) Malaysia through the Fundamental Research Grant Scheme (project code: FRGS/1/2019/STG01/UKM/02/2) and Universiti Kebangsaan Malaysia through the project code PP-SELFUEL-2023. The authors would like to express our sincere gratitude to the Malaysian Nuclear Agency and Centre for Research and Instrumentation Universiti Kebangsaan Malaysia (iCRIM) for providing the analysis facilities for this project.

References

- [1] A. Mahmood, N. Xie, B. Zhao, L. Zhong, Y. Zhang, L. Niu, Optimizing Surface N-Doping of Fe-N-C Catalysts Derived from Fe/Melamine-Decorated Polyaniline for Oxygen Reduction Electrocatalysis, *Advanced Materials Interfaces*, 8 (2021) 2100197. <https://doi.org/10.1002/admi.202100197>.
- [2] X. Zhang, Y.B. Mollamahale, D. Lyu, L. Liang, F. Yu, M. Qing, Y. Du, X. Zhang, Z.Q. Tian, P.K. Shen, Molecular-level design of Fe-N-C catalysts derived from Fe-dual pyridine coordination complexes for highly efficient oxygen reduction, *Journal of Catalysis*, 372 (2019) 245-257. <https://doi.org/10.1016/j.jcat.2019.03.003>.
- [3] L. Osmieri, A.H.A. Monteverde Videla, P. Ocón, S. Specchia, Kinetics of Oxygen Electroreduction on Me-N-C (Me = Fe, Co, Cu) Catalysts in Acidic Medium: Insights on the Effect of the Transition Metal, *The Journal of Physical Chemistry C*, 121 (2017) 17796-17817. 10.1021/acs.jpcc.7b02455.
- [4] A.E. Baumann, D.A. Burns, B. Liu, V.S. Thoi, Metal-organic framework functionalization and design strategies for advanced electrochemical energy storage devices, *Communications Chemistry*, 2 (2019) 86. 10.1038/s42004-019-0184-6.
- [5] Y. Deng, B. Chi, X. Tian, Z. Cui, E. Liu, Q. Jia, W. Fan, G. Wang, D. Dang, M. Li, K. Zang, J. Luo, Y. Hu, S. Liao, X. Sun, S. Mukerjee, g-C₃N₄ promoted MOF derived hollow carbon nanopolyhedra doped with high density/fraction of single Fe atoms as an ultra-high performance non-precious catalyst towards acidic ORR and PEM fuel cells, *Journal of Materials Chemistry A*, 7 (2019) 5020-5030. 10.1039/C8TA11785C.
- [6] Y. Wang, L. Chen, Y. Lai, Y. Wang, K. Wang, S. Song, MOF-Derived Porous Fe-N-C Materials for Efficiently Electrocatalyzing the Oxygen Reduction Reaction, *Energy & Fuels*, 36 (2022) 5415-5423. 10.1021/acs.energyfuels.2c00946.
- [7] J. Weiss, H. Zhang, P. Zelenay, Recent progress in the durability of Fe-N-C oxygen reduction electrocatalysts for polymer electrolyte fuel cells, *Journal of Electroanalytical Chemistry*, 875 (2020) 114696. <https://doi.org/10.1016/j.jelechem.2020.114696>.
- [8] Y. Huang, W. Liu, S. Kan, P. Liu, R. Hao, H. Hu, J. Zhang, H. Liu, M. Liu, K. Liu, Tuning morphology and structure of Fe-N-C catalyst for ultra-high oxygen reduction reaction activity, *International Journal of Hydrogen Energy*, 45 (2020) 6380-6390. <https://doi.org/10.1016/j.ijhydene.2019.12.130>.
- [9] S. Gupta, S. Zhao, O. Ogoke, Y. Lin, H. Xu, G. Wu, Engineering Favorable Morphology and Structure of Fe-N-C Oxygen-Reduction Catalysts through Tuning of Nitrogen/Carbon Precursors, *ChemSusChem*, 10 (2017) 774-785. <https://doi.org/10.1002/cssc.201601397>.
- [10] B. Liu, B. Huang, C. Lin, J. Ye, L. Ouyang, Porous carbon supported Fe-N-C composite as an efficient electrocatalyst for oxygen reduction reaction in alkaline and acidic media, *Applied Surface Science*, 411 (2017) 487-493. <https://doi.org/10.1016/j.apsusc.2017.03.150>.
- [11] X. Wu, W. Xie, X. Liu, X. Liu, Q. Zhao, in: *Catalysts*, 2022.
- [12] M. Naguib, M. Kurtoglu, V. Presser, J. Lu, J. Niu, M. Heon, L. Hultman, Y. Gogotsi, M.W. Barsoum, Two-Dimensional Nanocrystals Produced by Exfoliation of Ti₃AlC₂, *Advanced Materials*, 23 (2011) 4248-4253. <https://doi.org/10.1002/adma.201102306>.
- [13] J.A. Kumar, P. Prakash, T. Krithiga, D.J. Amarnath, J. Premkumar, N. Rajamohan, Y. Vasseghian, P. Saravanan, M. Rajasimman, Methods of synthesis, characteristics, and environmental applications of MXene: A comprehensive review, *Chemosphere*, 286 (2022) 131607. <https://doi.org/10.1016/j.chemosphere.2021.131607>.
- [14] C. Wei, L. Tan, Y. Zhang, B. Xi, S. Xiong, J. Feng, MXene/Organics Heterostructures Enable Ultrastable and High-Rate Lithium/Sodium Batteries, *ACS Applied Materials & Interfaces*, 14 (2022) 2979-2988. 10.1021/acsami.1c22787.

- [15] L. Ma, D. Luo, Y. Li, X. Chen, K. Wu, J. Xu, Y. Cao, M. Luo, I. Manke, F. Lai, C. Yang, Z. Chen, Architecture design of MXene-based materials for sodium-chemistry based batteries, *Nano Energy*, 101 (2022) 107590. <https://doi.org/10.1016/j.nanoen.2022.107590>.
- [16] X. Wang, X. Wang, J. Chen, Y. Zhao, Z. Mao, D. Wang, Durable sodium battery composed of conductive Ti₃C₂T_x MXene modified gel polymer electrolyte, *Solid State Ionics*, 365 (2021) 115655. <https://doi.org/10.1016/j.ssi.2021.115655>.
- [17] S. De, C.K. Maity, S. Sahoo, G.C. Nayak, Polyindole Booster for Ti₃C₂T_x MXene Based Symmetric and Asymmetric Supercapacitor Devices, *ACS Applied Energy Materials*, 4 (2021) 3712-3723. 10.1021/acsaem.1c00142.
- [18] H. Zhou, F. Wu, L. Fang, J. Hu, H. Luo, T. Guan, B. Hu, M. Zhou, Layered NiFe-LDH/MXene nanocomposite electrode for high-performance supercapacitor, *International Journal of Hydrogen Energy*, 45 (2020) 13080-13089. <https://doi.org/10.1016/j.ijhydene.2020.03.001>.
- [19] T. Liu, X. Liu, N. Graham, W. Yu, K. Sun, Two-dimensional MXene incorporated graphene oxide composite membrane with enhanced water purification performance, *Journal of Membrane Science*, 593 (2020) 117431. <https://doi.org/10.1016/j.memsci.2019.117431>.
- [20] A.K. Thakur, R. Sathyamurthy, R. Saidur, R. Velraj, I. Lynch, N. Aslfattahi, Exploring the potential of MXene-based advanced solar-absorber in improving the performance and efficiency of a solar-desalination unit for brackish water purification, *Desalination*, 526 (2022) 115521. <https://doi.org/10.1016/j.desal.2021.115521>.
- [21] C. Yang, Y. Luo, H. Lin, M. Ge, J. Shi, X. Zhang, Niobium Carbide MXene Augmented Medical Implant Elicits Bacterial Infection Elimination and Tissue Regeneration, *ACS Nano*, 15 (2021) 1086-1099. 10.1021/acsnano.0c08045.
- [22] E. Mostafavi, S. Irvani, MXene-Graphene Composites: A Perspective on Biomedical Potentials, *Nano-Micro Letters*, 14 (2022) 130. 10.1007/s40820-022-00880-y.
- [23] N.H. Ahmad Junaidi, W.Y. Wong, K.S. Loh, S. Rahman, W.R.W. Daud, A comprehensive review of MXenes as catalyst supports for the oxygen reduction reaction in fuel cells, *International Journal of Energy Research*, 45 (2021) 15760-15782. <https://doi.org/10.1002/er.6899>.
- [24] X. Xie, S. Chen, W. Ding, Y. Nie, Z. Wei, An extraordinarily stable catalyst: Pt NPs supported on two-dimensional Ti₃C₂X₂ (X = OH, F) nanosheets for oxygen reduction reaction, *Chemical Communications*, 49 (2013) 10112-10114. 10.1039/C3CC44428G.
- [25] H.B. Parse, I. Patil, B. Kakade, A. Swami, Cobalt Nanoparticles Encapsulated in N-Doped Carbon on the Surface of MXene (Ti₃C₂) Play a Key Role for Electroreduction of Oxygen, *Energy & Fuels*, 35 (2021) 17909-17918. 10.1021/acs.energyfuels.1c02486.
- [26] L. Jiang, J. Duan, J. Zhu, S. Chen, M. Antonietti, Iron-Cluster-Directed Synthesis of 2D/2D Fe–N–C/MXene Superlattice-like Heterostructure with Enhanced Oxygen Reduction Electrocatalysis, *ACS Nano*, 14 (2020) 2436-2444. 10.1021/acsnano.9b09912.
- [27] Q. Xue, Z. Pei, Y. Huang, M. Zhu, Z. Tang, H. Li, Y. Huang, N. Li, H. Zhang, C. Zhi, Mn₃O₄ nanoparticles on layer-structured Ti₃C₂ MXene towards the oxygen reduction reaction and zinc–air batteries, *Journal of Materials Chemistry A*, 5 (2017) 20818-20823. 10.1039/C7TA04532H.
- [28] L. Chen, Y. Lin, J. Fu, J. Xie, R. Chen, H. Zhang, Hybridization of Binary Non-Precious-Metal Nanoparticles with d-Ti₃C₂ MXene for Catalyzing the Oxygen Reduction Reaction, *ChemElectroChem*, 5 (2018) 3307-3314. <https://doi.org/10.1002/celec.201800693>.
- [29] Z. Li, Z. Zhuang, F. Lv, H. Zhu, L. Zhou, M. Luo, J. Zhu, Z. Lang, S. Feng, W. Chen, L. Mai, S. Guo, The Marriage of the FeN₄ Moiety and MXene Boosts Oxygen Reduction Catalysis: Fe 3d Electron Delocalization Matters, *Advanced Materials*, 30 (2018) 1803220. <https://doi.org/10.1002/adma.201803220>.

- [30] W. Gu, M. Wu, J. Xu, T. Zhao, MXene boosted metal-organic framework-derived Fe–N–C as an efficient electrocatalyst for oxygen reduction reactions, *International Journal of Hydrogen Energy*, 47 (2022) 17224–17232. <https://doi.org/10.1016/j.ijhydene.2022.03.229>.
- [31] W. Sudarsono, W.Y. Wong, K.S. Loh, E.H. Majlan, N. Syarif, K.-Y. Kok, R.M. Yunus, K.L. Lim, I. Hamada, Sengon wood-derived RGO supported Fe-based electrocatalyst with stabilized graphitic N-bond for oxygen reduction reaction in acidic medium, *International Journal of Hydrogen Energy*, 45 (2020) 23237–23253. <https://doi.org/10.1016/j.ijhydene.2020.05.158>.
- [32] H. Zhang, S. Hwang, M. Wang, Z. Feng, S. Karakalos, L. Luo, Z. Qiao, X. Xie, C. Wang, D. Su, Y. Shao, G. Wu, Single Atomic Iron Catalysts for Oxygen Reduction in Acidic Media: Particle Size Control and Thermal Activation, *Journal of the American Chemical Society*, 139 (2017) 14143–14149. 10.1021/jacs.7b06514.
- [33] Y. Zhao, W.-J. Jiang, J. Zhang, E.C. Lovell, R. Amal, Z. Han, X. Lu, Anchoring Sites Engineering in Single-Atom Catalysts for Highly Efficient Electrochemical Energy Conversion Reactions, *Advanced Materials*, 33 (2021) 2102801. <https://doi.org/10.1002/adma.202102801>.
- [34] D. Su, Y. Xiao, Y. Liu, S. Xu, S. Fang, S. Cao, X. Wang, Surface-confined polymerization to construct binary Fe₃N/Co–N–C encapsulated MXene composites for high-performance zinc-air battery, *Carbon*, 201 (2023) 269–277. <https://doi.org/10.1016/j.carbon.2022.09.007>.
- [35] X. Zhao, A. Vashisth, E. Prehn, W. Sun, S.A. Shah, T. Habib, Y. Chen, Z. Tan, J.L. Lutkenhaus, M. Radovic, M.J. Green, Antioxidants Unlock Shelf-Stable Ti₃C₂T_x (MXene) Nanosheet Dispersions, *Matter*, 1 (2019) 513–526. <https://doi.org/10.1016/j.matt.2019.05.020>.
- [36] Q. Xue, J.-b. Huang, D.-j. Yang, B. Li, C.-m. Zhang, Enhanced PEMFC durability with graphitized carbon black cathode catalyst supports under accelerated stress testing, *RSC Advances*, 11 (2021) 19417–19425. 10.1039/D1RA01468D.
- [37] M.M. El-Desoky, I. Morad, M.H. Wasfy, A.F. Mansour, Synthesis, structural and electrical properties of PVA/TiO₂ nanocomposite films with different TiO₂ phases prepared by sol–gel technique, *Journal of Materials Science: Materials in Electronics*, 31 (2020) 17574–17584. 10.1007/s10854-020-04313-7.
- [38] Y. Wen, C. Ma, Z. Wei, X. Zhu, Z. Li, FeNC/MXene hybrid nanosheet as an efficient electrocatalyst for oxygen reduction reaction, *RSC Advances*, 9 (2019) 13424–13430. 10.1039/C9RA01330J.
- [39] S.M. Saudid, S.K. Kamarudin, N.A. Karim, L.K. Shyuan, Superior stability and methanol tolerance of a metal-free nitrogen-doped hierarchical porous carbon electrocatalyst derived from textile waste, *Journal of Materials Research and Technology*, 11 (2021) 1834–1846. <https://doi.org/10.1016/j.jmrt.2021.01.089>.
- [40] R.B. Rakhi, B. Ahmed, M.N. Hedhili, D.H. Anjum, H.N. Alshareef, Effect of Postetch Annealing Gas Composition on the Structural and Electrochemical Properties of Ti₂CT_x MXene Electrodes for Supercapacitor Applications, *Chemistry of Materials*, 27 (2015) 5314–5323. 10.1021/acs.chemmater.5b01623.
- [41] L.E.I. Yanhua, N. Tan, Y. Zhu, H. Da, Y. Zhang, S. Sun, G. Gao, Synthesis of Porous N-Rich Carbon/MXene from MXene@Polypyrrole Hybrid Nanosheets as Oxygen Reduction Reaction Electrocatalysts, *Journal of the Electrochemical Society*, 167 (2020) 10.1149/1945-7111/aba15b.
- [42] E. Luo, M. Xiao, J. Ge, C. Liu, W. Xing, Selectively doping pyridinic and pyrrolic nitrogen into a 3D porous carbon matrix through template-induced edge engineering: enhanced catalytic activity towards the oxygen reduction reaction, *Journal of Materials Chemistry A*, 5 (2017) 21709–21714. 10.1039/C7TA07608H.

- [43] X. Fu, R. Gao, G. Jiang, M. Li, S. Li, D. Luo, Y. Hu, Q. Yuan, W. Huang, N. Zhu, L. Yang, Z. Mao, J. Xiong, A. Yu, Z. Chen, Z. Bai, Evolution of atomic-scale dispersion of Fe_Nx in hierarchically porous 3D air electrode to boost the interfacial electrocatalysis of oxygen reduction in PEMFC, *Nano Energy*, 83 (2021) 105734. <https://doi.org/10.1016/j.nanoen.2020.105734>.
- [44] S. Chen, X. Liang, S. Hu, X. Li, G. Zhang, S. Wang, L. Ma, C.-M.L. Wu, C. Zhi, J.A. Zapien, Inducing Fe 3d Electron Delocalization and Spin-State Transition of FeN₄ Species Boosts Oxygen Reduction Reaction for Wearable Zinc–Air Battery, *Nano-Micro Letters*, 15 (2023) 47. 10.1007/s40820-023-01014-8.
- [45] K. Kumar, T. Asset, X. Li, Y. Liu, X. Yan, Y. Chen, M. Mermoux, X. Pan, P. Atanassov, F. Maillard, L. Dubau, Fe–N–C Electrocatalysts' Durability: Effects of Single Atoms' Mobility and Clustering, *ACS Catalysis*, 11 (2021) 484-494. 10.1021/acscatal.0c04625.
- [46] J.D. Sinniah, W.Y. Wong, K.S. Loh, R.M. Yunus, S.N. Timmiati, Perspectives on carbon-alternative materials as Pt catalyst supports for a durable oxygen reduction reaction in proton exchange membrane fuel cells, *Journal of Power Sources*, 534 (2022) 231422. <https://doi.org/10.1016/j.jpowsour.2022.231422>.
- [47] M. Zhang, B. Yang, T. Yang, Y. Yang, Z. Xiang, A ferric citrate derived Fe-N-C electrocatalyst with stepwise pyrolysis for highly efficient oxygen reduction reaction, *Chinese Chemical Letters*, 33 (2022) 362-367. <https://doi.org/10.1016/j.ccllet.2021.06.054>.
- [48] M.F. Labata, G. Li, J. Ocon, P.-Y.A. Chuang, Insights on platinum-carbon catalyst degradation mechanism for oxygen reduction reaction in acidic and alkaline media, *Journal of Power Sources*, 487 (2021) 229356. <https://doi.org/10.1016/j.jpowsour.2020.229356>.
- [49] X. Yang, Y. Zeng, W. Alnoush, Y. Hou, D. Higgins, G. Wu, Tuning Two-Electron Oxygen-Reduction Pathways for H₂O₂ Electrosynthesis via Engineering Atomically Dispersed Single Metal Site Catalysts, *Advanced Materials*, 34 (2022) 2107954. <https://doi.org/10.1002/adma.202107954>.
- [50] H. Chen, Y. Wen, Y. Qi, Q. Zhao, L. Qu, C. Li, Pristine Titanium Carbide MXene Films with Environmentally Stable Conductivity and Superior Mechanical Strength, *Advanced Functional Materials*, 30 (2020) 1906996. <https://doi.org/10.1002/adfm.201906996>.
- [51] R.R. Raja Sulaiman, A. Hanan, W.Y. Wong, R. Mohamad Yunus, K. Shyuan Loh, R. Walvekar, V. Chaudhary, M. Khalid, in: *Catalysts*, 2022.
- [52] C. Xu, L. Chen, Y. Wen, S. Qin, H. Li, Z. Hou, Z. Huang, H. Zhou, Y. Kuang, A co-operative protection strategy to synthesize highly active and durable Fe/N co-doped carbon towards oxygen reduction reaction in Zn–air batteries, *Materials Today Energy*, 21 (2021) 100721. <https://doi.org/10.1016/j.mtener.2021.100721>.
- [53] W.-T. Wang, N. Batool, T.-H. Zhang, J. Liu, X.-F. Han, J.-H. Tian, R. Yang, When MOFs meet MXenes: superior ORR performance in both alkaline and acidic solutions, *Journal of Materials Chemistry A*, 9 (2021) 3952-3960. 10.1039/D0TA10811A.
- [54] X.-L. Chen, H.-B. Zhu, L.-F. Ding, Cu dopant triggering remarkable enhancement in activity and durability of Fe-N-C electrocatalysts toward oxygen reduction, *Journal of Electroanalytical Chemistry*, 873 (2020) 114389. <https://doi.org/10.1016/j.jelechem.2020.114389>.
- [55] Y. Sha, J. Ji, S. Li, X. Gao, B. Zhang, M. Ling, C. Liang, Z. Lin, Atomic Platinum Anchored on Fe-N-C Material for High Performance Oxygen Reduction Reaction, *European Journal of Inorganic Chemistry*, 2020 (2020) 165-168. <https://doi.org/10.1002/ejic.201901027>.
- [56] X. Yan, X. Li, C. Fu, C. Lin, H. Hu, S. Shen, G. Wei, J. Zhang, Large specific surface area S-doped Fe–N–C electrocatalysts derived from Metal–Organic frameworks for oxygen

- reduction reaction, *Progress in Natural Science: Materials International*, 30 (2020) 896-904. <https://doi.org/10.1016/j.pnsc.2020.10.018>.
- [57] G. Yang, J. Zhu, P. Yuan, Y. Hu, G. Qu, B.-A. Lu, X. Xue, H. Yin, W. Cheng, J. Cheng, W. Xu, J. Li, J. Hu, S. Mu, J.-N. Zhang, Regulating Fe-spin state by atomically dispersed Mn-N in Fe-N-C catalysts with high oxygen reduction activity, *Nature Communications*, 12 (2021) 1734. 10.1038/s41467-021-21919-5.
- [58] S. Luo, J. Hu, S. Guo, D. Yu, P. Dong, M. Xu, L. Han, M. Li, Y. Lin, F. Liu, C. Zhang, Y. Zhang, Ionic liquid-derived Fe, N, S, F multiple heteroatom-doped carbon materials for enhanced oxygen reduction reaction, *Nanotechnology*, 32 (2021) 395701. 10.1088/1361-6528/ac0c40.
- [59] J. Liu, C. Fan, G. Liu, L. Jiang, MOF-derived dual metal (Fe, Ni) –nitrogen–doped carbon for synergistically enhanced oxygen reduction reaction, *Applied Surface Science*, 538 (2021) 148017. <https://doi.org/10.1016/j.apsusc.2020.148017>.
- [60] N. Xue, Y. Zhang, C. Wang, X. Xue, D. Ouyang, H. Zhu, J. Yin, Enhancing oxygen reduction reaction performance in acidic media via bimetal Fe and Cr synergistic effects, *International Journal of Hydrogen Energy*, 47 (2022) 33979-33987. <https://doi.org/10.1016/j.ijhydene.2022.07.266>.
- [61] Z. Li, X. Liang, Q. Gao, H. Zhang, H. Xiao, P. Xu, T. Zhang, Z. Liu, Fe, N co-doped carbonaceous hollow spheres with self-grown carbon nanotubes as a high performance binary electrocatalyst, *Carbon*, 154 (2019) 466-477. <https://doi.org/10.1016/j.carbon.2019.08.036>.
- [62] J.-C. Li, H. Zhong, M. Xu, T. Li, L. Wang, Q. Shi, S. Feng, Z. Lyu, D. Liu, D. Du, S.P. Beckman, X. Pan, Y. Lin, M. Shao, Boosting the activity of Fe-N_x moieties in Fe-N-C electrocatalysts via phosphorus doping for oxygen reduction reaction, *Science China Materials*, 63 (2020) 965-971. 10.1007/s40843-019-1207-y.
- [63] A.A.P.R. Perera, K.A.U. Madhushani, B.T. Punchihewa, A. Kumar, R.K. Gupta, in: *Materials*, 2023.
- [64] L. Sun, Y. Qin, Y. Yin, ZIF derived PtCo alloys-based nitrogen-doped Graphene as cathode catalyst for proton exchange membrane fuel cell, *Journal of Power Sources*, 562 (2023) 232758. <https://doi.org/10.1016/j.jpowsour.2023.232758>.